



## OPEN ACCESS

APPROVED BY  
Frontiers Editorial Office,  
Frontiers Media SA, Switzerland

\*CORRESPONDENCE  
Frontiers Production Office  
✉ production.office@frontiersin.org

RECEIVED 22 August 2023  
ACCEPTED 22 August 2023  
PUBLISHED 01 September 2023

CITATION  
Frontiers Production Office (2023) Erratum:  
AMPA and GABAA receptor nanodomains  
assemble in the absence of synaptic  
neurotransmitter release.  
*Front. Mol. Neurosci.* 16:1281653.  
doi: 10.3389/fnmol.2023.1281653

COPYRIGHT  
© 2023 Frontiers Production Office. This is an  
open-access article distributed under the terms  
of the [Creative Commons Attribution License  
\(CC BY\)](#). The use, distribution or reproduction  
in other forums is permitted, provided the  
original author(s) and the copyright owner(s)  
are credited and that the original publication in  
this journal is cited, in accordance with  
accepted academic practice. No use,  
distribution or reproduction is permitted which  
does not comply with these terms.

# Erratum: AMPA and GABAA receptor nanodomains assemble in the absence of synaptic neurotransmitter release

Frontiers Production Office\*

Frontiers Media SA, Lausanne, Switzerland

## KEYWORDS

Synapse, neurotransmitter release, postsynaptic neurotransmitter receptors, AMPA receptor, GABA receptor, excitatory, inhibitory, nanodomain

## An Erratum on

[AMPA and GABAA receptor nanodomains assemble in the absence of synaptic neurotransmitter release](#)

by Ramsay, H. J., Gookin, S. E., Ramsey, A. M., Kareemo, D. J., Crosby, K. C., Stich, D. G., Olah, S. S., Actor-Engel, H. S., Smith, K. R., and Kennedy, M. J. (2023). *Front. Mol. Neurosci.* 16:1232795. doi: 10.3389/fnmol.2023.1232795

Due to a production error, there was a mistake in the legends for [Figures 2–4](#) as published. The requested changes were missed during typesetting. The correct legends appear below.

The publisher apologizes for this mistake. The original article has been updated.

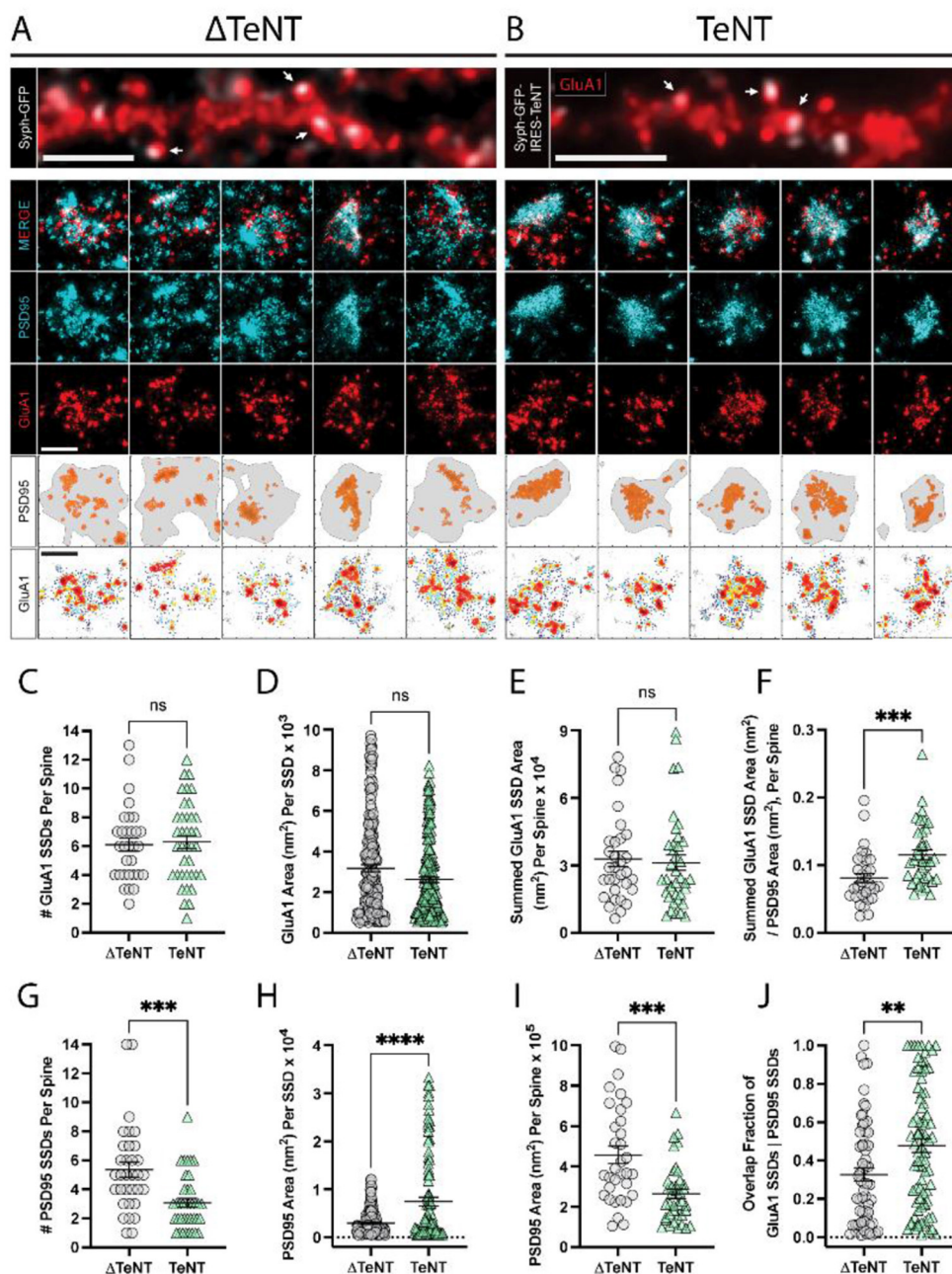


FIGURE 2

Formation of excitatory receptor and scaffold SSDs in the absence of neurotransmission. (A, B) Representative epifluorescence images of dendritic regions for cultures infected with control virus ( $\Delta$ TeNT, A), or TeNT virus (TeNT, B) and stained for surface GluA1 (red) are shown (top panels) with syph-GFP, or syph-GFP-IRES-TeNT shown in greyscale. In both cases note the apposition of syph-GFP signal and GluA1-positive (red) dendritic spines (white arrows). Scale bar = 5  $\mu$ m in each image. Representative dSTORM images of synapses contacted by  $\Delta$ TeNT (A), or TeNT (B) terminals are shown below in rows 2–4. Row 5 shows the PSD boundary for each synapse, defined by a minimum PSD95 localization density (gray borders), with PSD95 localizations in defined SSDs rendered in orange. Row 6 shows GluA1 localization density maps for each synapse with warmer colors representing higher GluA1 localization density. Scale bars in rows 4 and 6 both = 500 nm. (C) There was no significant difference in the number of GluA1 SSDs per spine at TeNT-silenced synapses compared to controls [spines,  $n = 31 \Delta$ TeNT/38 TeNT; ns, not significant;  $p = 0.7690$  (*T*-Test)]. (D) The area of individual GluA1 SSDs was not significantly different at TeNT-silenced synapses compared to controls [SSDs,  $n = 194 \Delta$ TeNT/200 TeNT; ns, not significant;  $p = 0.0531$  (Mann–Whitney)]. (E) The summed GluA1 SSD area, per spine was not significantly different at TeNT-silenced synapses compared to controls [spines,  $n = 32 \Delta$ TeNT/38 TeNT; ns, not significant;  $p = 0.5777$  (Mann–Whitney)]. (F) The ratio between the summed GluA1 SSD area to its total PSD95 area was significantly increased at TeNT-contacted dendritic spines [spines,  $n = 33 \Delta$ TeNT/37 TeNT; \*\*\* $p < 0.001$ ;  $p = 0.0007$  (Mann–Whitney)]. (G) The number of PSD95 SSDs per spine was significantly decreased at TeNT-contacted spines compared to controls [spines,  $n = 33 \Delta$ TeNT/38 TeNT; \*\*\* $p < 0.001$ ;  $p = 0.0002$  (Mann–Whitney)]. (H) The area of individual PSD95 SSDs was significantly increased at TeNT-silenced spines compared to controls [SSDs,  $n = 141 \Delta$ TeNT/103 TeNT; \*\*\*\* $p < 0.0001$  (Welch’s *T*-Test)]. (I) The total PSD95 area per spine was significantly reduced at TeNT-contacted spines compared to controls [spines,  $n = 33 \Delta$ TeNT/38 TeNT; \*\*\* $p = 0.0001$  (Mann–Whitney)]. (J) The degree of GluA1 SSD/PSD95 SSD overlap was significantly increased at TeNT-contacted spines compared to controls [SSDs,  $n = 61 \Delta$ TeNT/81 TeNT; \*\* $p < 0.01$ ;  $p = 0.0052$  (Mann–Whitney)].

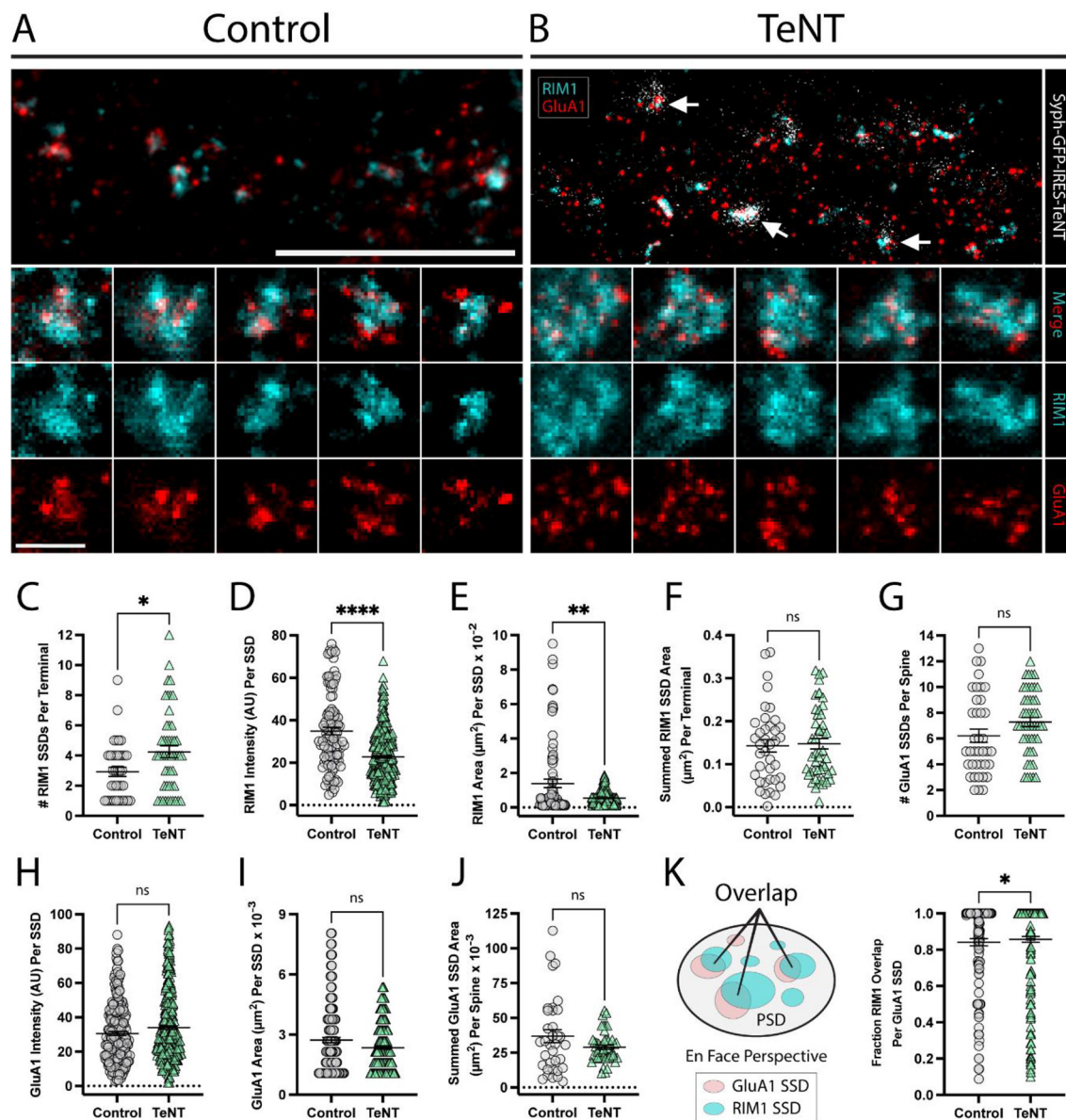


FIGURE 3

Trans-synaptic SSD alignment is intact at chronically silenced excitatory synapses. (A, B) Representative STED images of synapses labeled with RIM1 (cyan) and GluA1 (red) for (control, A) and (TeNT, B) conditions. Note the apposition of syph-GFP signal and GluA1-positive (red) dendritic spines (white arrows). Scale bar = 5  $\mu\text{m}$ . Columns 1–5 in (A, B) display representative STED images of synapses for control (A), and TeNT (B) conditions; merged RIM1 (cyan), and GluA1 (red) (row 2); RIM1 (cyan) (row 3); GluA1 (red) (row 4). Scale bar = 500 nm. (C) The number of RIM1 SSDs per synaptic terminal was significantly increased at TeNT-expressing terminals compared to controls [terminals,  $n = 38$  control/49 TeNT;  $*p < 0.05$  (Mann–Whitney)]. (D) RIM1 fluorescence intensity quantified at individual SSDs was decreased at TeNT-silenced terminals compared to controls [SSDs,  $n = 104$  control/346 TeNT; \*\*\*\* $p < 0.0001$  (Mann–Whitney)]. (E) The area of individual RIM1 SSDs was decreased at TeNT-silenced terminals compared to controls [SSDs,  $n = 81$  control/281 TeNT; \*\* $p < 0.01$  (Welch’s  $T$ -Test)]. (F) The summed RIM1 SSD area per terminal was not significantly different at TeNT-silenced terminals compared to controls [terminals,  $n = 38$  control/48 TeNT; ns, not significant;  $p = 0.7050$  (Mann–Whitney)]. (G) The number of GluA1 SSDs per spine was not significantly different at TeNT-silenced spines compared to controls [spines,  $n = 38$  control/49 TeNT; ns, not significant;  $p = 0.0539$  (Mann–Whitney)]. (H) The fluorescence intensity of individual GluA1 SSDs was not significantly different at TeNT-silenced spines compared to controls [SSDs,  $n = 218$  control/372 TeNT; ns, not significant;  $p = 0.0959$  (Mann–Whitney)]. (I) The mean area of individual GluA1 SSDs was not significantly different at TeNT-silenced spines compared to controls [SSDs,  $n = 187$  control/339 TeNT; ns, not significant;  $p = 0.2098$  (Mann–Whitney)]. (J) The summed GluA1 SSD area per spine was not significantly different at TeNT-silenced spines compared to controls [spines,  $n = 35$  control/49 TeNT; ns, not significant;  $p = 0.1120$  (Welch’s  $T$ -Test)]. (K) Schematic showing the fraction of GluA1/RIM1 SSD overlap (left). GluA1 SSD overlap with RIM1 SSDs was slightly elevated at TeNT-associated synapses (i.e., on average, a larger area of each GluA1 SSD at TeNT-associated synapses was overlapped by closely-associated RIM1 SSDs) [SSDs,  $n = 155$  Control/268 TeNT;  $*p < 0.05$ ;  $p = 0.0372$  (Mann–Whitney)].



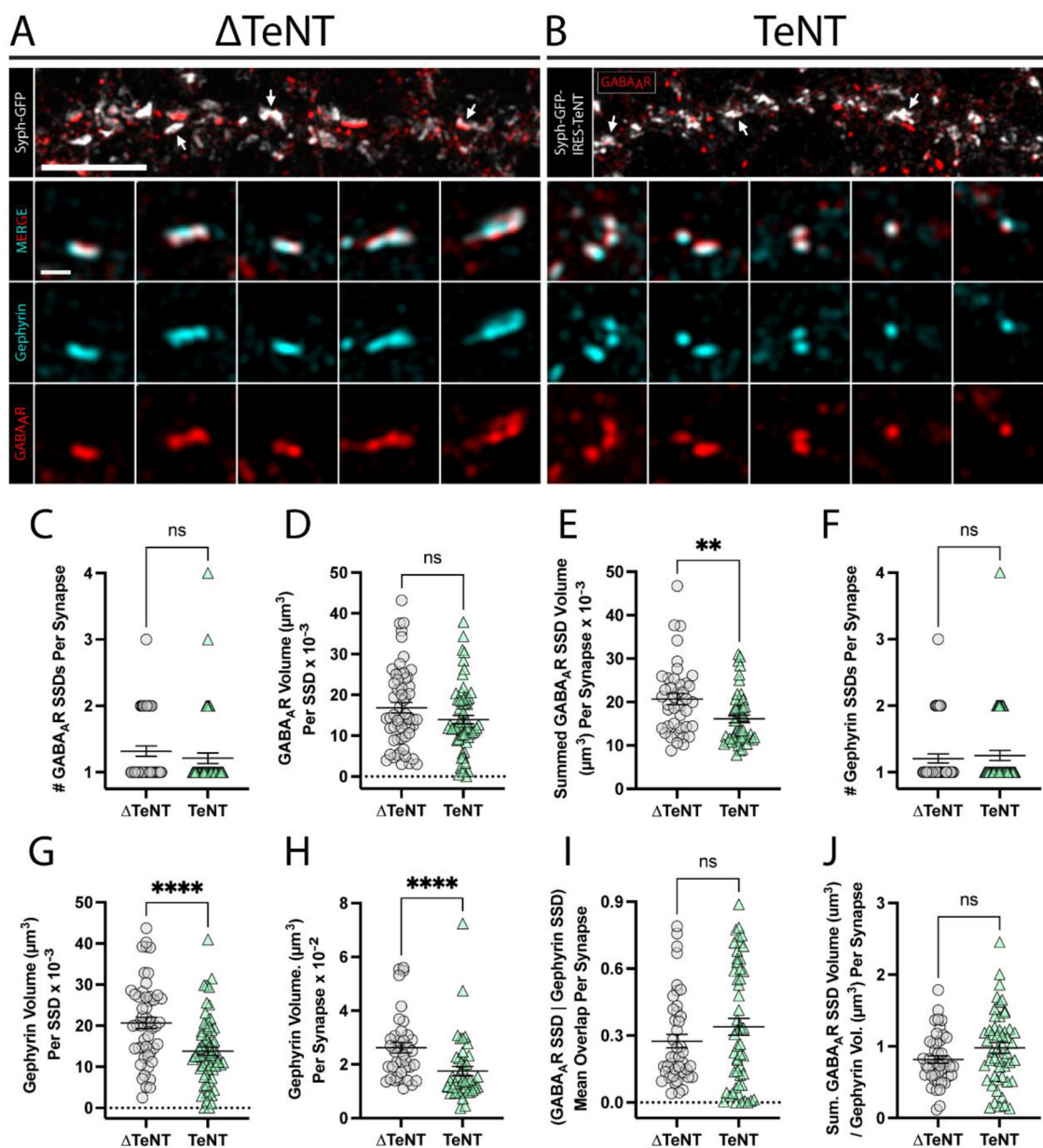


FIGURE 4

Formation of inhibitory receptor and scaffold SSDs in the absence of neurotransmission. (A, B) Representative SIM images of dendritic regions from ( $\Delta$ TeNT, A) or (TeNT, B), cultures displaying syph-GFP, or syph-GFP-IRES-TeNT (greyscale), and GABAAR (red). Note the apposition of syph-GFP signal and GABAAR-positive (red) synapses (white arrows). Scale bar = 5  $\mu$ m. Columns 1–5 display representative synapses for  $\Delta$ TeNT (A), and TeNT (B) conditions; merged gephyrin (cyan), and GABAAR (red) (row 2); gephyrin (cyan) and GABAAR (red) (row 3); and GABAAR (red) (row 4). Scale bar = 500 nm. (C) The number of GABAAR SSDs per synapse was not significantly different at TeNT-silenced synapses compared to controls [synapses,  $n = 44 \Delta$ TeNT/52 TeNT; ns, not significant;  $p = 0.1340$  (Mann–Whitney)]. (D) The volume of individual GABAAR SSDs was not significantly different at TeNT-silenced synapses compared to controls [SSDs,  $n = 57 \Delta$ TeNT/63 TeNT; ns, not significant;  $p = 0.0739$  (Mann–Whitney)]. (E) The summed synaptic volume of GABAAR SSDs per synapse was significantly decreased at TeNT-silenced synapses compared to controls [synapses,  $n = 41 \Delta$ TeNT/50 TeNT; \*\* $p < 0.01$ ;  $p = 0.0020$  (Mann–Whitney)]. (F) The number of gephyrin SSDs per synapse was not significantly different at TeNT-silenced synapses compared to controls [synapses,  $n = 44 \Delta$ TeNT/52 TeNT; ns, not significant;  $p = 0.7200$  (Mann–Whitney)]. (G) The volume of individual gephyrin SSDs was significantly reduced at TeNT-silenced synapses compared to controls [SSDs,  $n = 52 \Delta$ TeNT/64 TeNT; \*\*\*\* $p < 0.0001$  ( $T$ -Test)]. (H) The total gephyrin SSDs was significantly decreased at TeNT-silenced synapses compared to controls [synapses,  $n = 38 \Delta$ TeNT/44 TeNT; \*\*\*\* $p < 0.0001$  (Mann–Whitney)]. (I) There was no significant difference in the mean overlap between GABAAR SSDs and gephyrin SSD signals at TeNT-silenced synapses compared to controls [SSDs,  $n = 43 \Delta$ TeNT/52 TeNT; ns, not significant;  $p = 0.5039$  (Mann–Whitney)]. (J) The ratio between the summed synaptic volume of GABAAR SSDs, and the total gephyrin volume, per synapse was not significantly different at TeNT-silenced synapses compared to controls [synapses,  $n = 44 \Delta$ TeNT/51 TeNT; ns, not significant;  $p = 0.0795$  ( $T$ -Test)].